University of Nebraska - Lincoln

DigitalCommons@University of Nebraska - Lincoln

2021

Magnetoelectric coupling at the Ni/Hf0.5Zr0.5O2 interface

A. Dmitriyeva, V. Mikheev, S. Zarubin, A. Chouprik, G. Vinai, V. Polewczyk, P. Torelli, Y. Matveyev, C. Schlueter, I. Karateev, Q. Yang, Z. Chen, L.L. Tao, E. Y. Tsymbal, and A. Zenkevich

Magnetoelectric Coupling at the Ni/Hf$_{0.5}$Zr$_{0.5}$O$_2$ Interface

Anna Dmitriyeva, Vitalii Mikheev, Sergei Zarubin, Anastasia Chouprik, Giovanni Vinai,
Vincent Polewczyk, Piero Torelli, Yury Matveyev, Christoph Schlueter, Igor Karateev, Qiong Yang,
Zhaojin Chen, Lingling Tao, Evgeny Y. Tsymbal,* and Andrei Zenkevich*

Read Online

ACCESS | Metrics & More | Article Recommendations | SI Supporting Information

ABSTRACT: Composite multiferroics containing ferroelectric and ferromagnetic components often have much larger magneto-electric coupling compared to their single-phase counterparts. Doped or alloyed HfO$_2$-based ferroelectrics may serve as a promising component in composite multiferroic structures potentially feasible for technological applications. Recently, a strong charge-mediated magnetoelectric coupling at the Ni/HfO$_2$ interface has been predicted using density functional theory calculations. Here, we report on the experimental evidence of such magnetoelectric coupling at the Ni/Hf$_{0.5}$Zr$_{0.5}$O$_2$(HZO) interface. Using a combination of *operando* XAS/XMCD and HAXPES/MCDAD techniques, we probe element-selectively the local magnetic properties at the Ni/HZO interface in functional Au/Co/Ni/HZO/W capacitors and demonstrate clear evidence of the ferroelectric polarization effect on the magnetic response of a nanometer-thick Ni marker layer. The observed magnetoelectric effect and the electronic band lineup of the Ni/HZO interface are interpreted based on the results of our theoretical modeling. It elucidates the critical role of an ultrathin NiO interlayer, which controls the sign of the magnetoelectric effect as well as provides a realistic band offset at the Ni/HZO interface, in agreement with the experiment. Our results hold promise for the use of ferroelectric HfO$_2$-based composite multiferroics for the design of multifunctional devices compatible with modern semiconductor technology.

KEYWORDS: *ferroelectric HfO$_2$, Hf$_{0.5}$Zr$_{0.5}$O$_2$, composite multiferroics, magnetoelectric coupling, operando spectroscopy, XMCD, MCDAD*
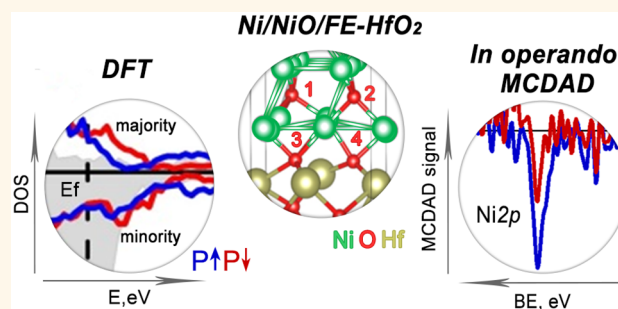
M ultiferroic materials with coexisting ferroelectric and ferromagnetic orders have attracted much attention due to the magnetoelectric (ME) coupling, opening alternative prospects for electronic devices.[1,2] Switching magnetization by applied electric rather than magnetic field or spin-polarized current requires much less energy,[3−5] making multiferroics promising for memory and logic applications.[6,7] Due to a limited number of single-phase multiferroic compounds operating at room temperature, composite multiferroics containing ferroelectric (FE) (or piezoelectric) and ferromagnetic components have been considered as viable candidates.[8−11] It was shown that composite multiferroic materials often have much larger ME coupling compared to their single-phase counterparts, resulting from strain-mediated,[12−15] charge-mediated,[16−22] ion migration,[23] and even morphological changes[24,25] as coupling mechanisms.

Over the last several years, ME multiferroic materials have been assessed for technological applications, with a wide range of available materials[2] and possible implementations as spin−orbit logic units.[26] Within these efforts, however, the challenge

is the compatibility with silicon-based technologies. Ferroelectricity discovered in doped or alloyed hafnia (HfO$_2$) films[27,28] has stimulated significant efforts in studying their relevant properties.[29−35] These studies have demonstrated the applicability of ferroelectric hafnia to nonvolatile memory devices, such as FE random access memory (FeRAM),[36] FE field-effect transistors (FeFETs),[37,38] and FE tunnel junctions (FTJs).[39−41]
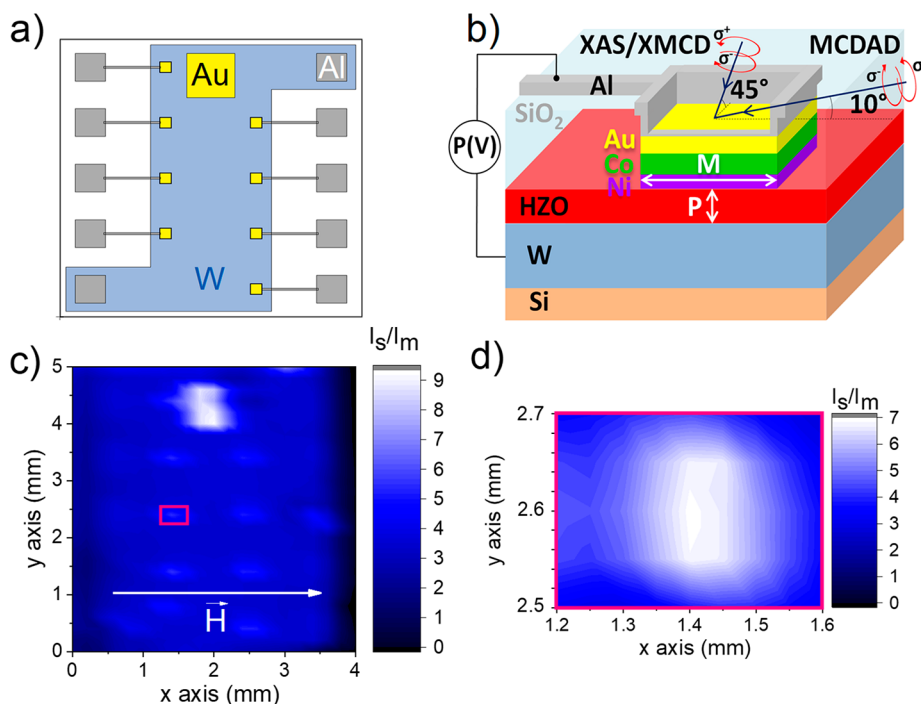
Furthermore, due to the excellent isolating properties, ferroelectricity persisting down to a few nanometer thickness,[42,43] and good compatibility with the Si-based semiconductor process,[37,38,42,44] doped hafnia thin films are

Figure 1. Layout of the chip with the patterned Au/Co/Ni/FE-HZO/W capacitor devices prepared for operando synchrotron measurements (a); schematic drawing of a single capacitor device structure used in *operando* XAS/XMCD and HAXPES/MCDAD measurements (b); image of the chip with contact areas obtained by TEY at the Co L_3 edge (c) (the color scale corresponds to the sample current I_S normalized to the incident photon flux measured before the endstation I_m); zoom-in of the area marked in (c), displaying the top contact area to the device $\sim 200 \times 200 \ \mu m^2$ in size (d).

expected to serve as a promising FE component in multiferroic heterostructures potentially feasible for technological applications. In this regard, exploring the ME effect at the ferroelectric/ferromagnetic interface in the heterostructures comprising doped HfO_2 as a FE constituent[45] is crucial for searching alternative composite multiferroics compatible with Si technology.

Recently, a strong charge-mediated ME coupling at the Ni/ HfO_2 interface driven by FE HfO_2 polarization reversal has been predicted using density functional theory (DFT) calculations.[46] Depending on the polarization orientation, a sizable difference in the interfacial Ni−O bonding as well as screening charges was found, which affected the relative population of the exchange-split majority- and minority-spin bands at the interface and eventually gave rise to significant changes of the interfacial magnetic moments.

Motivated by this theoretical prediction, in this work, we explore and provide the experimental evidence of the ME coupling effect at the interface between an ultrathin ferromagnetic Ni layer and an alloyed $Hf_{0.5}Zr_{0.5}O_2$ (HZO) thin film, a representative HfO_2-based ferroelectric.[28] Using the combination of X-ray synchrotron-based spectroscopic techniques, such as X-ray magnetic circular dichroism (XMCD)[47] and magnetic circular dichroism in angular distribution (MCDAD),[48] we probe element-selectively the local magnetic properties at the Ni/HZO interface in functional Au/Co/Ni/HZO/W capacitors. *In situ* electric biasing of the sample during the XMCD and MCDAD measurements allows for monitoring directly and reproducibly the effect of FE polarization switching on the magnitude and/or orientation of the magnetic moment of the marker Ni layer at the interface at the atomic scale. The results of the performed *operando* measurements demonstrate clear evidence of the ME coupling

at the Ni/HZO interface driven by HZO polarization reversal. To get insight into the chemical/electronic and structural properties of the Ni/HZO interface, we additionally employ the complementary hard X-ray photoemission spectroscopy (HAXPES) and high-resolution transmission electron microscopy (HRTEM) combined with electron energy-loss spectroscopy (EELS). To elucidate the origin of the observed ME effect, theoretical modeling based on DFT calculations is performed for different Ni/HfO_2 interface terminations. An excellent agreement between the theory and the experiment is obtained in the sign and the magnitude of the ME effect as well as in the electronic band lineup, assuming the presence of a monolayer-thick NiO interlayer at the Ni/HfO_2 interface.

RESULTS/DISCUSSION

In order to probe the ME coupling effect at the Ni/HZO interface *in operando* by synchrotron-based spectroscopic techniques, we fabricated Si chips with functional FE capacitors using the previously developed methodology (Figure 1a).[44,49,50] Thicknesses (given in nanometers) of individual layers in the stack Au(3)/Co(1.5−2.5)/Ni(1.5)/HZO(10)/W(20) were carefully optimized to enable the probing of buried Ni interfacial properties both by XMCD and MCDAD. A 1.5 or 2.5 nm thick Co layer was deposited on top of Ni to stabilize ferromagnetism and thus enable XMCD and MCDAD responses at room temperature, respectively. The Co/Ni ferromagnetic layer was capped *in situ* with Au to prevent oxidation. The layered structure was further annealed to crystallize a FE HZO phase (details on the growth and patterning of the multilayered structure are given in the Experimental Section). The layout of the capacitor device used for *operando* XMCD and MCDAD measurements is shown in Figure 1b, while Figure 1c and d display the images of a full
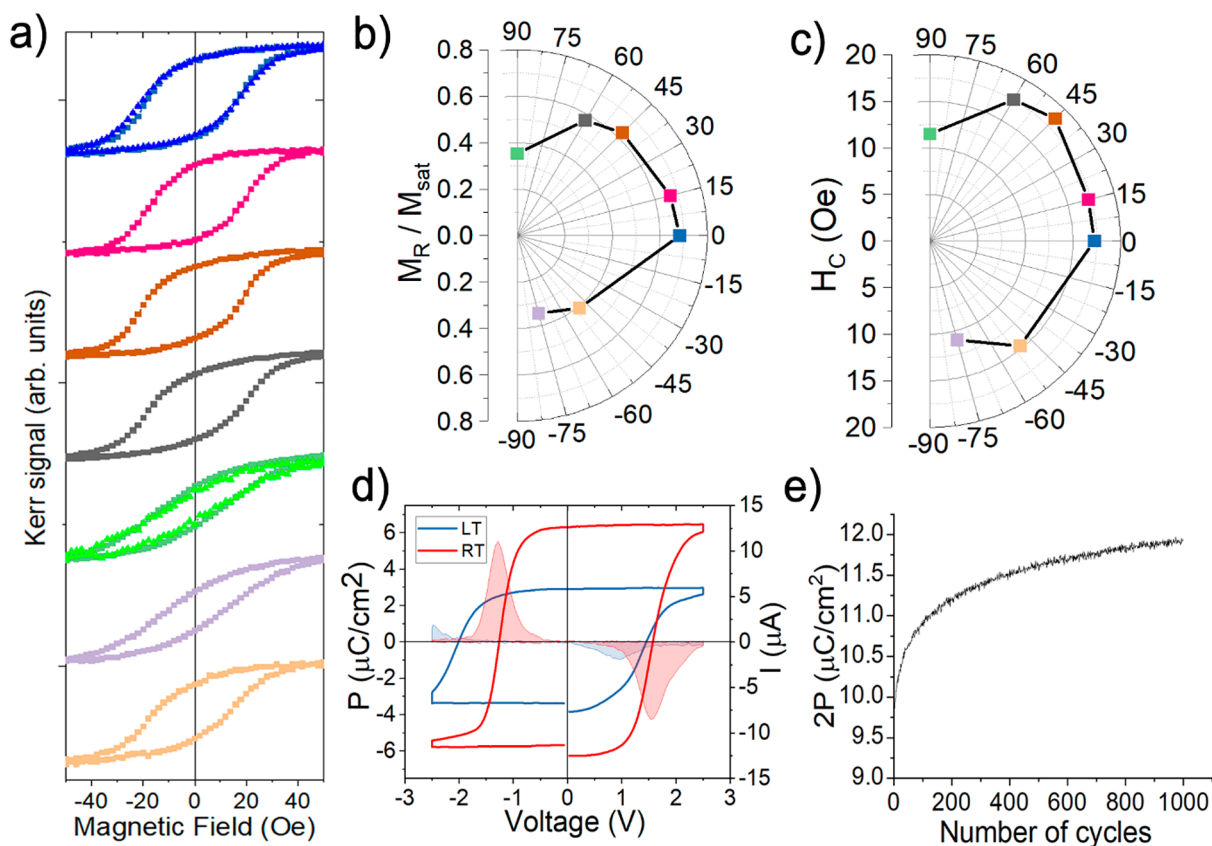
Figure 2. Angular MOKE distribution (a) of the Co/Ni/HZO sample applying a magnetic field in-plane. Squares refer to a full film sample, while triangles (blue and green) to a 800 μm lateral size chip. Polar plots of the normalized magnetic remanence (b) and the coercive magnetic field (c); polarization *vs* voltage and corresponding current *vs* voltage curves (d) for the Au/Co/Ni/HZO/W ferroelectric capacitor at room temperature (RT) and at $T \approx 100$ K (LT) as derived from *in situ* pulsed switching during XMCD and MCDAD experiments, respectively; the plot of polarization as a function of the number of switching cycles (e) performed in order to "wake-up" the ferroelectric prior to *operando* measurements.

chip obtained by measuring the total electron yield (TEY) at the Co L_3 edge with the top contact as well as a selected contact of the Au/Co/Ni/HZO/W capacitor device under investigation, respectively (see the Methods/Experimental section for details on the spectroscopic setups).

The magnetic properties of as-prepared samples were first characterized *ex situ* using the magneto-optical Kerr effect (MOKE). Figure 2a shows the magnetic hysteresis loops of the Co(2.5)/Ni(1.5) bilayer measured at room temperature. Here, the loops measured on the full film (square dots) are compared to those measured on a patterned square sample with a lateral size of $800 \times 800 \ \mu m^2$ (triangles), showing no obvious changes in the anisotropic behavior between the two cases. The magnetic remanence M_R normalized to the magnetic saturation M_{sat} and the coercive field H_c are shown using polar plots in Figure 2b and c, respectively. The sample presents signs of uniaxial anisotropy, with the easy axis along x (0°) and the hard one along y (+90°) directions as shown in Figure 1b, which could be attributed to extrinsic factors such as shadowing effects or residual strains, particularly critical in ultrathin layers.[51] During X-ray absorption spectroscopy (XAS)/X-ray magnetic circular dichroism (XMCD) and HAXPES/MCDAD measurements, the magnetic field was applied in the sample plane along the 0° direction (as shown in Figure 1,c), *i.e.*, along the magnetic easy axis of the sample.

The FE properties of the capacitor devices on the chip prepared for *operando* XMCD and MCDAD experiments were characterized both *ex situ* and *in situ* using pulsed switching methodology known as positive-up-negative-down (PUND).[52] The polarization (2P) *vs* voltage (V) curves as measured by applying +2.5/−2.5 V at room temperature (RT) and low ($T \approx 100$ K) temperature (LT) upon the "wake-up" 10^3 switching cycles are shown in Figure 2d and e, respectively. The coercive electric fields $E_c \approx$ + 1.55/−1.25 MV·cm^{-1} (~+1.45/−2.0 MV·cm^{-1}) and the remnant polarization $2P \approx 12 \ \mu C/cm^2$ (~8 $\mu C/cm^2$) are obtained at room (low) temperature.

We note that the polarization values obtained in our ferroelectric capacitor devices during the *operando* experiments are significantly smaller than those obtained on the probe station. This is due to our experimental conditions, in particular, large RC values limiting the switching pulse duration. The reduced polarization value at LT compared to that at RT is likely due to the different protocol that we used in these measurements. While the RT measurements were performed shortly after initial "wake-up" cycling, the LT measurements were performed after cooling the sample for several hours. The latter led to the pronounced fluid imprint effect,[53] which is the signature of nonferroelectric charges. The resulting shift of the I−V curve with respect to the +2.5/−2.5 V range used during the polarization switching gave rise to a much smaller current response at LT compared to RT (represented by dashed blue and red areas, respectively, in Figure 2d), which ultimately limited polarization switching in our experiment at LT.
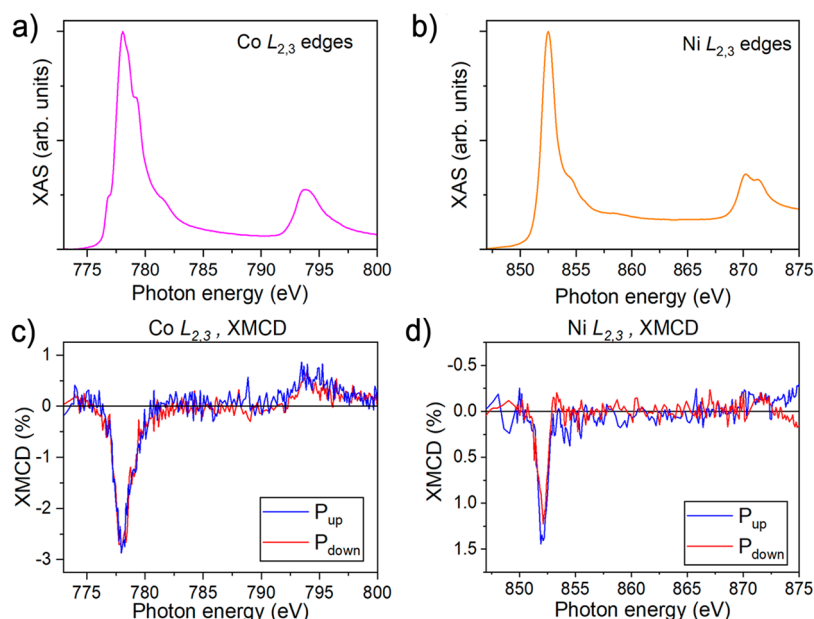
Figure 3. XAS (a, b) and XMCD (c, d) room temperature *operando* measurements at Co (a, c) and Ni (b, d) $L_{2,3}$ edges on the Au(3)/Co(1.5)/Ni(1.5)/HZO(10)/W(50) capacitor device. Both XAS spectra are shown in P_{up} state. In (c) and (d), the dichroic signals are recorded upon *in situ* out-of-plane ferroelectric polarization switching down (red) or up (blue).
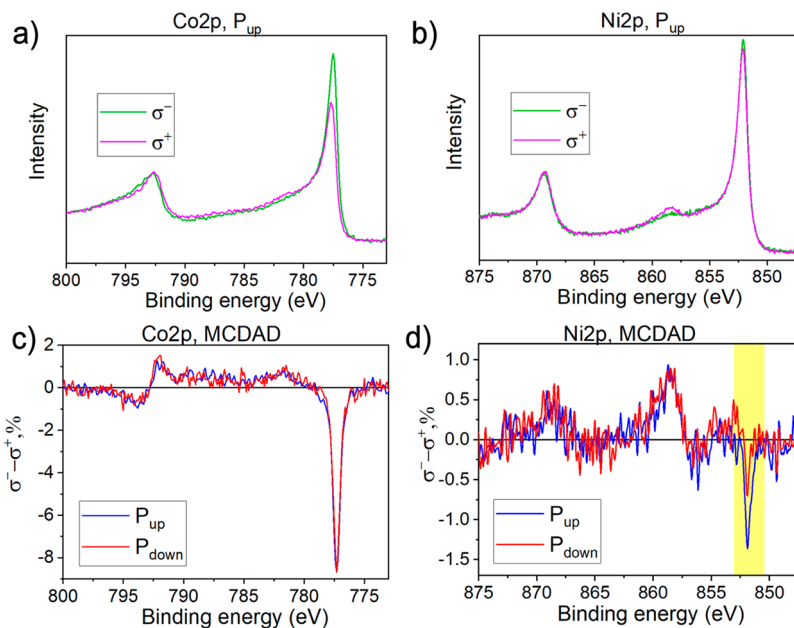
Figure 4. Ni 2p (a) and Co 2p (b) core level lines taken at LT for σ^+ and σ^- circular polarization of X-rays demonstrating the MCDAD effect (at a particular orientation of FE polarization). The effect of ferroelectric polarization switching on MCDAD signal for Ni 2p (c) and Co 2p (d) core level lines (yellow stripe marks the spectral region over which the signal was integrated).

The precharacterized sample was used for the XAS and XMCD *operando* analysis performed at room temperature. Figure 3 displays the absorption spectra at Co and Ni $L_{2,3}$ edges measured on the 200×200 μm^2 contact of the selected electrically wired capacitor device on the chip. Both Co (Figure 3a) and Ni (Figure 3b) show signs of partial oxidation of the ferromagnetic layer. The Co absorption spectrum has features at the L_3 edge, indicating some degree of oxidation,[54,55] while the Ni spectrum reveals an additional contribution to the line shape, which can be attributed to the presence of Ni^{2+} (*i.e.*, NiO)[56] overlapped with its metallic fingerprint.[57] By fitting the Ni spectrum with the combination

of the reference Ni^0 and Ni^{2+} lines recorded at the same beamline (Figure S1), subtracting the background, and normalizing the total thickness of the Ni/NiO layer to 1.5 nm, we obtain 1.0 and 0.5 nm for the Ni and NiO sublayer thickness, respectively. Nonetheless, both elements exhibit a clear dichroic signal at room temperature coming from the metallic part,[57,58] whose intensity is reduced due to the partial oxidation. *In situ* switching of the HZO polarization orientation in the Au(3)/Co(1.5)/Ni(1.5)/HZO(10)/W(20) capacitor affects the intensity of the dichroic signal at Ni L_3 edges. As it can be seen in Figure 3d, the intensity of the dichroic signal at the Ni L_3 edge is different when measured for

polarization up (P_{up}, blue curve) and down (P_{down}, red curve), going from 1.44% to 1.22%. At the same time, the Co dichroic signal measured during the same FE polarization switching cycles shows no detectable change within the limit of instrumental resolution (Figure 3c). It is important to emphasize that during the XMCD (as well as MCDAD) measurements no external voltage was applied; the only source of the electric field affecting the magnetic signal was ferroelectric charges of opposite signs depending on polarization orientation.

A very similar sample, but with a thicker (∼2.5 nm) Co layer, was further characterized by the MCDAD technique,[48] which is complementary to HAXPES.[59,60] The MCDAD signal was measured at the Co 2p and Ni 2p energy regions at LT temperature. The typical spectra after the normalization for σ^+ and σ^- polarized X-rays for a particular orientation of ferroelectric polarization are presented in Figure 4,a,b. Since the σ^+ and σ^- polarization of X-rays was achieved in the setup by a diamond phase retarder, the incoming intensity for both polarizations varied within ∼20%. To compensate for this effect, the spectra were collected for two opposite polarization orientations (P_{up} and P_{down}) and two opposite directions of the magnetic field ($H_{\rightarrow}$ and $H_{\leftarrow}$). The final MCDAD signal was calculated as

$$\text{MCDAD} = (I_{\sigma^+,H_{\underrightarrow{\quad}}} + I_{\sigma^-,H_{\underleftarrow{\quad}}}) - (I_{\sigma^-,H_{\underrightarrow{\quad}}} + I_{\sigma^+,H_{\underleftarrow{\quad}}})$$

Figure 4c,d show the resulting MCDAD signals for the Co 2p and Ni 2p lines, which confirm the ferromagnetic properties of both Co and Ni layers. Furthermore, the MCDAD signals for the Ni 2p line are clearly different for two opposite ferroelectric polarization orientations switched *in situ* (blue and red spectra for P_{up} and P_{down}, respectively, in Figure 4c), in contrast to the MCDAD data for the Co 2p line, where no effect of polarization reversal is observed (Figure 4d), in full coherence with the XMCD measurements shown in Figure 3. To ensure that the observed effect is not related to the drift of experimental parameters, four sequential MCDAD measurements were performed, and each pair of measurements for opposite polarizations of X-rays was analyzed separately. The results shown in Figure S3 confirm that the observed effect of the FE polarization reversal on the magnitude of the magnetic signal at the Ni/HZO interface is reproducible.

In order to quantify the observed effect, we integrated the area under the MCDAD spectra over the binding energy range E_B = 850.5−853 eV (marked in yellow in Figure 4d and Figure S3). The obtained values are $\Sigma_{P\uparrow} \approx - 0.21$ and $\Sigma_{P\downarrow} \approx - 0.04$ for the upward and downward polarization, respectively (the values derived from separate sequential measurements in Figure S3 are given in Table S1). It is worth noting that the same MCDAD experiments performed also at room temperature did not yield any convincing effect beyond the experimental error. This is attributed to the smaller observed MCDAD signal compared to the XMCD at the employed experimental conditions (particularly, the nonoptimal geometry for MCDAD).

In order to correlate the observed effect of the FE polarization on the magnetic moment at the Ni/HZO interface with the theory described below, we further characterized chemical, electronic, and structural properties of the Ni/HZO interface. In particular, a fraction of oxidized Ni was observed in the Ni 2p core-level spectrum (see Figure S2) and in Ni $L_{2,3}$ edges (see Figure 3,b). By analyzing the relative peak intensities of the metallic and oxidized Ni in the Ni 2p

spectrum, we estimated the thickness of the oxidized Ni layer to be about 0.35 nm out of the total Ni layer thickness of 1.5 nm (see details in Supporting Information, Section 2), in reasonable agreement with the estimates obtained from the XAS data. This may be due to either a redox reaction at the Ni/HZO interface (which could occur during the rapid thermal annealing of the stack to crystallize the FE HZO phase) and/or the discontinuity of the Au overlayer. Using the well-known XPS-based methodology,[61,62] we reconstructed the electronic band alignment diagram of the Co/Ni/HZO/W device structure as shown in Figure 5 (details described in
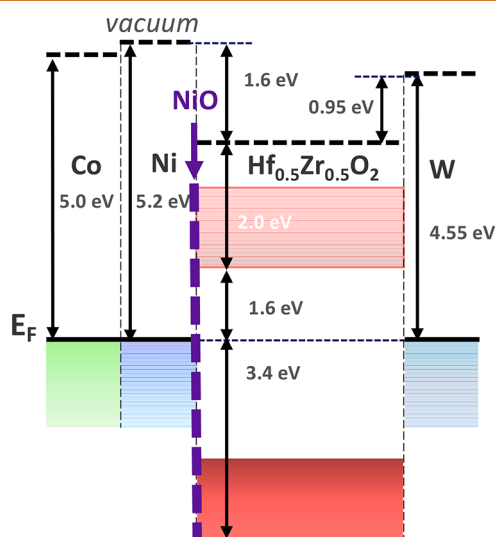

Figure 5. Reconstructed electronic band alignment diagram across the Co/Ni/HZO/W device structure.

Supporting Information, Section 2). We found that a very large barrier ΔE = 1.6 eV is built-up at the Ni/HZO interface, representing the electric dipole with negative charges accumulated at the Ni side. These negative charges originate from the unbound electrons resulting from oxygen vacancies formed in HZO due to the redox reaction at the Ni/HZO interface. They are expected to affect the relative population of the exchange-split majority- and minority-spin bands at the interfacial Ni layer irrespective of FE polarization orientation.

The structural properties of the Au/Co/Ni/HZO/W stack cut from the capacitor subjected to *operando* measurements were analyzed by HRTEM in combination with EELS. The high-resolution dark-field image of the sample cross section shown in Figure 6a reveals, as expected, the polycrystalline structure of the Ni, Co, and HZO layers and the rather rough, within a few monolayers, interface. The EELS elemental maps shown in Figure 6b confirm an atomically sharp Ni/HZO interface, in contrast to that between Ni and Co, which is found to be rather diffuse. A closer look at the metallic grains adjacent to the HZO layer and a careful structural analysis (described in the Supporting Information, Section 4) reveal that Ni and Co are partially intermixed, with the alloyed grains forming a common layer. Such alloying occurs during the rapid thermal annealing process aiming at the crystallization of the FE phase in the as-grown HZO layer. These grains possess an *fcc* structure (Figure S4 in the Supporting Information) as expected for a Ni−Co alloy.[63] EELS profiling across such Ni−Co grains (Figure 6b) indicates a strong gradient of Ni concentration, with the edge in contact with HZO dominated in
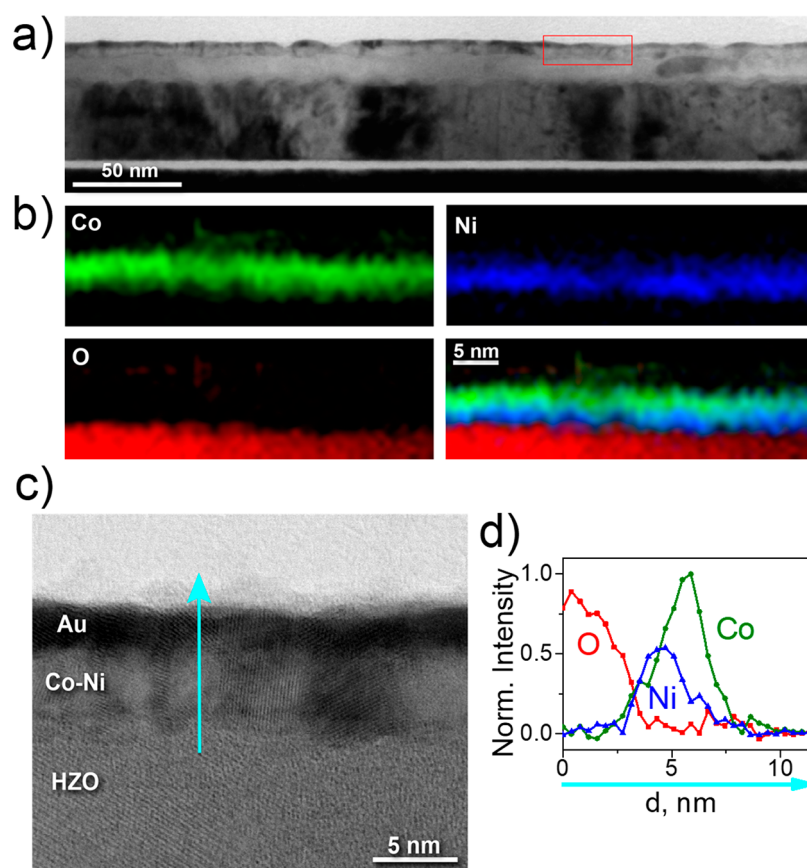
Figure 6. TEM/EELS analysis of the Co/Ni/HZO/W device structure. STEM image of the device structure (a); EELS maps of Co, Ni, and O and a combined map (b); HR STEM image of the device structure (c); and EELS profiles for Co, Ni, and O (d).

by Ni and the upper part adjacent to the Au capping layer being pure Co. In addition, we find that the capping layer of Au may also penetrate between Co−Ni ferromagnetic grains down to the HZO layer (but do not intermix, due to the immiscibility gap upon annealing at T = 400 °C).[64]

To correlate our experimental data with theory, we investigate the ME effect and the band alignment between Ni and HfO_2 using DFT calculations, as described in Computational Methods. In the calculations, following the previous theoretical work,[46] we first consider the atomic structure of the Ni/HfO_2 interface, as shown in Figure 7a. In this O-terminated structure, the number of O atoms at the interface is assumed to be the same as within a HfO_2 layer in the bulk (i.e., four O atoms corresponding to a quarter of the bulk unit cell). We refer to this interface structure as IS-1. Figure 7b shows the calculated layer-projected density of states (LDOS) across the $Ni/HfO_2/Ni$ heterostructure, where each panel corresponds to the LDOS of Ni (yellow) and HfO_2 (cyan) layers. The region with zero LDOS within HfO_2 corresponds to the energy band gap (which is somewhat underestimated in comparison to the experimental value of about 5.0 eV[42] due to the well-known deficiency of DFT). The position of the Fermi energy (E_F) with respect to the valence band maximum (E_V) determines the valence band offset (VBO) between Ni and HfO_2. As seen from Figure 7b, the obtained VBO for the IS-1 structure is about 1.4 eV, which is much smaller than the experimental value of 3.4 eV (see Figure 5).

This disagreement can be understood in terms of the interface structure, which is far from being perfect in our

experiment. Despite this difference in the atomic structure, our model calculations allow obtaining more insights regarding the interface stoichiometry. Since the VBO is expected to be very sensitive to the number of oxygen atoms at the interface, we calculate the electronic structure of the Ni/HfO_2 interface with a reduced O concentration. Due to oxygen electronegativity, removing O atoms from the interface is expected to push the HfO_2 bands deeper in energy and thus to enhance the VBO between Ni and HfO_2. This expectation is confirmed by our DFT calculations. Figure 7c (left) shows a Ni/HfO_2 interface, referred to as IS-2, where two O atoms are removed from the original interface (atoms O1, O4 at the bottom interface and atoms O6, O7 at the top interface in Figure 7a). The calculated LDOS for this $Ni/HfO_2/Ni$ heterostructure (Figure 7,c, right) demonstrates that the VBO is pushed up to 3.2 eV above the VBM, which is in excellent agreement with the experimental value of 3.4 eV.

The oxygen stoichiometry of the Ni/HfO_2 interface in the IS-2 structure where two O atoms per lateral HfO_2 unit cell (or equivalently one O atom per one Hf atom) are present at the interface seems to be reasonable from the point of view of the HfO_2 surface polarity and stoichiometry. We assume the nominal oxygen valence of O^{2-} and hafnium of Hf^{4+} in HfO_2 make the HfO_2 (001) surface polar if there are two O atoms per one Hf atom at the surface. On the other hand, having one O atom per one Hf atom makes the HfO_2 (001) surface nonpolar and stoichiometric. This concentration of oxygen on the HfO_2 surface and hence on the Ni/HfO_2 interface in the IS-2 structure is therefore expected to provide lower formation energy due to the absence of the energetically unfavorable
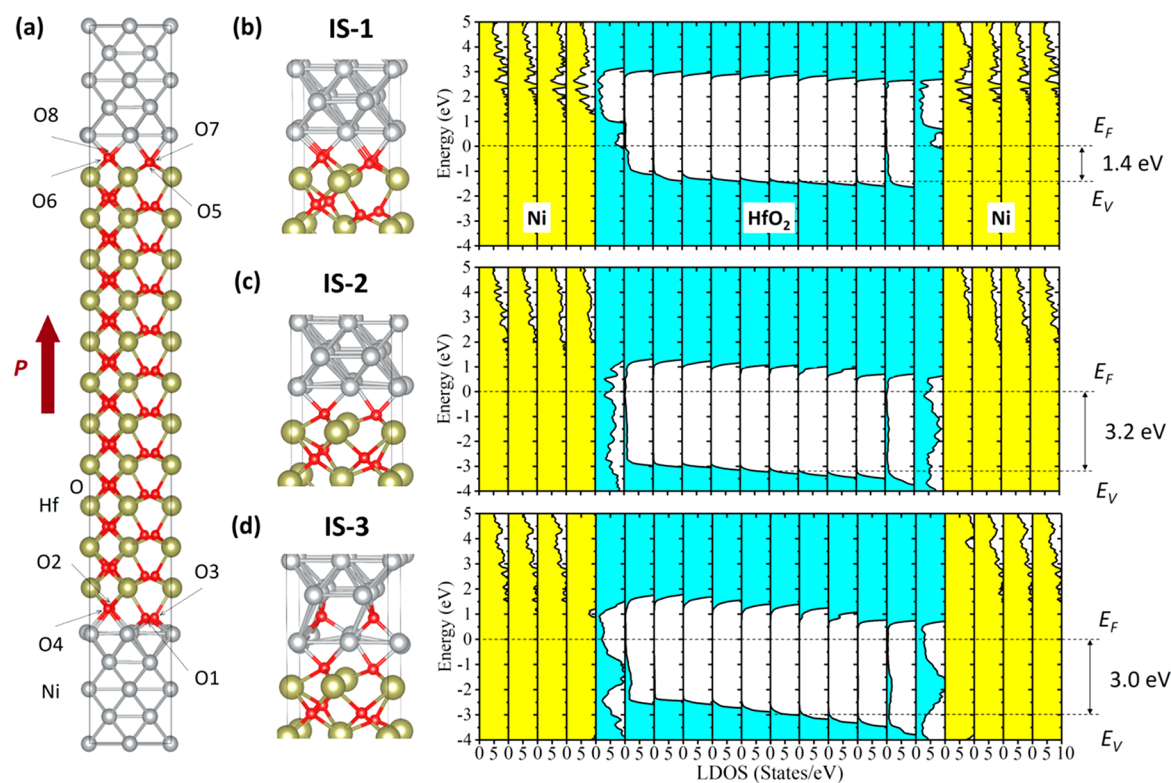
Figure 7. Ni/HfO$_2$ initial atomic structure (a) used for the calculation of the band alignment and the magnetoelectric effect (Hf, green; O, red; Ni, gray). O1−O8 denote the interfacial O atoms. The polarization (P) is pointing up. Three different Ni/HfO$_2$ interface structures (b−d) IS-1, IS-2, and IS-3 (left) and corresponding layer-projected density of states (LDOS) (right); IS-1 (b) with four O atoms at each interface (the same as (a)). IS-2 (c) with O1, O4 at the bottom interface and O6, O7 at the top interface removed. IS-3 (d) with O1, O4 at the bottom interface and O6, O7 at the top interface placed within the interfacial Ni layer. Band offsets between the Fermi energy (E_F) and the valence band maximum (E_V) are indicated in (b)−(d).

electric field associated with a polar surface (interface). This statement is valid for any type of interface and therefore likely valid for the Ni/HfO$_2$ interface stoichiometry in our experiment.

To explore the ME effect at the Ni/HfO$_2$ interface, we calculate the total interfacial magnetic moments for different interfacial configurations described above (*i.e.*, IS-1 and IS-2). Assuming the symmetric interface terminations in the Ni/HfO$_2$/Ni heterostructure allows us to examine the magnetic properties of the Ni/HfO$_2$ (001) interface for polarization pointing into the Ni layer (P_{up}) or away from it (P_{down}) using the same structural model with unidirectional polarization of HfO$_2$ (Figure 7a). The results for the calculated interfacial magnetic moments are displayed in Table 1. We see clear differences in the magnetic moments, Δm, between P_{up} or P_{down} polarization directions (*i.e.*, between top and bottom interfaces in Figure 7a). For example, for the IS-1 interface, Δm contributed by the interfacial Ni atoms is about 0.18 μ_B per Ni atom, which is enhanced up to 0.27 μ_B after including the contribution from the interfacial O atoms. Removing interfacial O suppresses the interfacial magnetoelectric effect as seen from the monotonic decrease of Δm with the reducing O concentration (compare IS-1 to IS-2 in Table 1). For IS-1 and IS-2 structures, the magnetic moments for polarization pointing into the Ni layer (P_{up}) are smaller than those for polarization pointing away (P_{down}).

This observation can be qualitatively explained from the analysis of spin-resolved density of states (DOS) projected on the interfacial Ni atoms, which is shown in Figure 8a,b. The

Table 1. Interfacial Magnetic Moments m and Magnetic Moment Difference $\Delta m = m(P_{down}) − m(P_{up})$ (in Units of μ_B, per Ni Atom) for Three Different Interface Structures, IS-1, IS-2, and IS-3, for Polarization of HfO$_2$ Pointing into the Ni Layer (P_{up}) and Away from It (P_{down})[a]

	IS-1		IS-2		IS-3	
	Ni + O	Ni	Ni + O	Ni	Ni + O	Ni
m (P_{down})	1.24	1.03	0.62	0.59	0.17	0.12
m (P_{up})	0.97	0.85	0.44	0.43	0.29	0.23
Δm	0.27	0.18	0.18	0.16	−0.12	−0.11

[a]"Ni" and "Ni + O" represent the magnetic moments contributed by the interfacial Ni atoms and by both Ni and O atoms, respectively. Interface structure IS-3 consistent with the experimental results is marked with gray color.

interface magnetization difference between the P_{up} and P_{down} polarizations can be understood in terms of the screening charges. Since the minority-spin DOS dominates around the Fermi energy, at the P_{up} interface, accumulation of the minority-spin electrons (blue line) reduces the magnetic moment of Ni, whereas at the P_{down} interface, depletion of the minority-spin electrons (red line) enhances the magnetic moment of Ni, as was discussed in ref 46. Decreasing the O concentration at the interface reduces the HfO$_2$ surface polarity and thus both the Ni interfacial magnetic moment and its change with respect to polarization orientation.
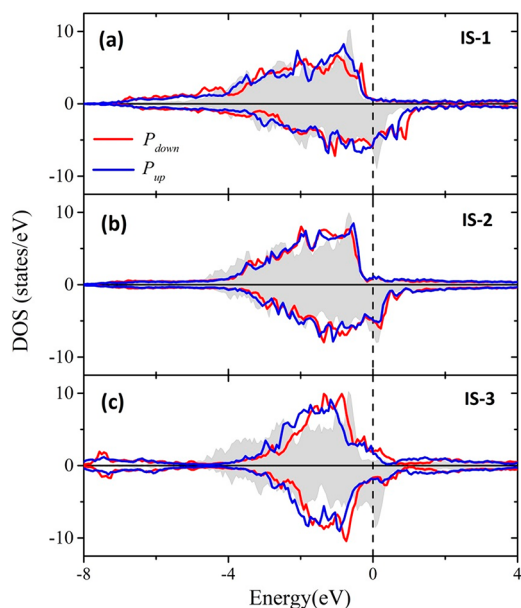
Figure 8. Spin-resolved density of state (DOS) at the interfacial Ni atoms at the Ni/HfO$_2$ interfaces for polarization pointing into the Ni layer (P_{up}) or away from it (P_{down}) for the IS-1 interface (a), IS-2 interface (b), and IS-3 interface (c). The majority- and minority-spin DOS are plotted in the top (positive) and bottom (negative) panels, respectively. The gray-filled curves represent the DOS of the central atomic layers (bulk) of Ni atoms. The vertical dashed line indicates the Fermi energy (E_F).

While this ME effect is in general consistent with the previous results for ferromagnet/ferroelectric interfaces (see, for example, ref 65), its sign is opposite that found in our experiments. Specifically, the calculated interfacial magnetic moment is larger for P_{down} than for Pup, whereas our MCDAD and XMCD data suggest the opposite. This "reversal" of the ME effect can be attributed to the formation of an ultrathin NiO layer near the interface during the heterostructure fabrication process. The oxidized Ni layer is expected to form Ni−O bonding and antibonding states, which modify the electronic structure of the interface responsible for the ME effect. In particular, the antibonding states may appear at the Fermi energy and reverse the spin polarization on the interfacial Ni DOS (similarly to the case of oxidized Co),[66,67] which would reverse the ME effect compared to the ideal interface.

To explore the effect of the interfacial NiO, we therefore construct an IS-3 structure, where two O atoms are moved inside the interfacial Ni layers forming a NiO layer, as shown in the left panel of Figure 7d. The calculated LDOS (Figure 7d, right) reveals the Fermi energy lying 3.0 eV above the VBM, which is in good agreement with the experimentally measured VBO of 3.4 eV. The calculated ME effect is opposite those of the IS-1 and IS-2 structures, as seen from the negative value of Δm in Table 1. Such a reversed ME effect can be understood from the analysis of the spin-resolved DOS shown in Figure 8c. While for the IS-1 and IS-2 structures (Figure 8a,b), the minority-spin DOS dominates around the Fermi energy, for the IS-3 structure the majority-spin DOS is larger than the minority-spin DOS. This behavior originates from the exchange-split Ni−O antibonding states positioned near the Fermi energy. As a result, for polarization pointing into the Ni layer (P_{up}), accumulation of the majority-spin electrons (blue

line) enhances the magnetic moment of Ni, whereas for polarization pointing away from the Ni layer (P_{down}), depletion of the majority-spin electrons (red line) reduces the magnetic moment of Ni, which results in the reversed ME effect.

CONCLUSIONS

In conclusion, stimulated by the recent theoretical prediction of a strong charge-mediated ME coupling at the Ni/HfO$_2$ interface driven by FE HfO$_2$ polarization reversal, we have employed the combination of two complementary synchrotron-based techniques, XMCD and MCDAD, to probe element-selectively the local magnetic properties at the Ni/Hf$_{0.5}$Zr$_{0.5}$O$_2$ interface in functional FE capacitors. We have demonstrated clear evidence of the FE polarization effect on the magnetic response of a nanometer-thick Ni marker layer both at room and low (∼100 K) temperature. The observed ME effect as well as the reconstructed electronic band lineup at the Ni/Hf$_{0.5}$Zr$_{0.5}$O$_2$ interface have been interpreted based on the performed theoretical modeling, which took into account the realistic interface stoichiometry. In particular, the critical role of a monolayer thick NiO interlayer has been elucidated, which reverses the sign of the magnetic response on FE polarization orientation as well as provides a realistic band offset at the Ni/Hf$_{0.5}$Zr$_{0.5}$O$_2$ interface, in agreement with the experiment. It is reasonable to suggest that the charge-mediated ME coupling effect observed in polycrystalline bilayers would be much stronger in heteroepitaxial structures employing FE HfO$_2$ and ferromagnetic electrode(s) with a structurally perfect interface, and our results will hopefully encourage performing further studies in this direction. For the more distant future, the demonstrated ME coupling effects hold promise for the use of FE HfO$_2$-based composite multiferroics for the design of multifunctional devices compatible with the modern semiconductor technology.

METHODS/EXPERIMENTAL

Sample Fabrication. A 40-nm-thick W layer was deposited by magnetron sputtering on Si chips 1.5 × 1.5 cm^2 in size. An HZO layer of 10 nm in thickness was grown by atomic layer deposition on top. The HZO growth process has been described in detail previously.[42,49] Ni, Co, and Au layers were then deposited by pulsed laser deposition at room temperature in a single vacuum cycle at thicknesses 1.5, 2, and 2.5 nm, respectively. Thicknesses were carefully optimized to fit the requirements for XMCD and MCDAD experiments, being 1.5 nm for the former and 2.5 nm for the latter to maximize the signal sensitivity of both measurements, and checked by Rutherford backscattering spectrometry. In order to stabilize the non-centrosymmetric orthorhombic phase, the as-grown structures were subjected to rapid thermal annealing at $T = 400$ °C in an argon atmosphere. To ensure in situ pulsed switching and polarization measurements by the remote source-meter unit, the Al pads ∼0.25 mm^2 in size connected to the capacitor devices tope electrodes were also fabricated on the chip. The contact to the common bottom W electrode was provided by a large square Al pad 1 × 1 mm^2 in size on top of the HZO layer.

Ferroelectric Characterization. The ferroelectric properties of the fabricated Au/Co/Ni/Hf$_{0.5}$Zr$_{0.5}$O$_2$/W capacitors were first examined ex situ using a Cascade Summit 1100 probe-station coupled with an Agilent B1500A semiconductor device analyzer. The ferroelectric properties were also controlled in situ during XAS/XMCD and HAXPES/MCDAD analysis with an Agilent B2912A source-measure unit by implementing the PUND technique.[50] In order to reverse in situ the electrical polarization of the HZO layer, electrically isolated sample holders were used,[22,24,68] with a gold wire silver pasted to the common bottom electrode and the top electrode of the selected capacitor device. The two contacts were then

connected to the source-meter, which allowed obtaining $I(V)$ curves and eventually to derive $P(V)$ loops.[69]

Magneto-Optic Kerr Effect. Longitudinal MOKE measurements were performed at room temperature, at the NFFA-Trieste infrastructure of IOM-CNR[51] using an *s*-polarized red laser (658 nm) and a photoelastic modulator at 50 kHz. The laser spot was reduced with a focusing lens and an optical shutter to obtain a spot ∼500 μm in diameter on the sample.

X-ray Absorption Spectroscopy and X-ray Magnetic Circular Dichroism Measurements. XAS and XMCD measurements were taken at the APE-HE beamline at Elettra Sincrotrone[70] in TEY mode, normalizing at each photon energy the sample current intensity (I_S) by the current measured on a mesh placed at the entrance of the endstation (I_m), corresponding to the intensity of the incident photon flux. Absorption spectra at Co and Ni $L_{2,3}$ edges were taken at both room and low temperature, in circular polarization with an incident angle of 45°. Two orthogonal mechanical slits at the refocusing level of the beamline were used to minimize the spot dimension on the sample down to ∼100 μm in diameter. The XMCD measurements were recorded at ±5 Oe, after reversing the sample magnetization at each energy point with an external in-plane magnetic field pulse of ±200 Oe, large enough to saturate the magnetization of the devices. The intensity of the dichroic signal was normalized to the sum of the two XA spectra, taking into account the angle of incidence of 45° and a 75% degree of light polarization.

Magnetic Circular Dichroism in the Angular Distribution. *Operando* MCDAD of photoelectrons in hard X-ray photoemission[48] was measured at the P22 beamline at PETRA III (DESY, Hamburg).[60] HAXPES spectra were collected with a Specs 225 HV analyzer choosing an excitation energy $E = 6$ keV with an overall energy resolution of about 0.2 eV. The spectra were acquired in short-circuit configurations, with both electrodes kept grounded. The 10° incident X-ray beam angle configuration was selected to maximize both MCDAD effect and photoelectrons intensity. The samples were aligned to ensure the easy magnetization axis to be along the X-ray beam. An external magnetic field of ∼1000 Oe was applied by approaching an external permanent magnet toward the sample between spectra measurements, while during the measurements the magnet was retracted. In order to facilitate the magnetoelectric coupling effect, the samples were cooled to a temperature $T \approx 100$ K.

Scanning Transmission Electron Microscopy (STEM) and Electron Energy Loss Spectroscopy. The sample cross section aimed at the STEM/EELS analysis was cut from the capacitor device structure by the focused ion beam technique. STEM measurements were performed with an S/TEM Titan 80-300 (Thermo Fisher Scientific) microscope equipped with a Cs probe corrector, an energy-dispersive X-ray spectrometer, an EELS system (Gatan), and a high-angle annular dark-field detector (Fischione). The microscope was operated at 300 kV.

Computational Methods. To explore the band alignment between Ni and HfO_2, we construct $Ni/HfO_2/Ni$ heterostructures by stacking 5.75 unit-cell layers of HfO_2 and nine monolayers of *fcc* Ni along the (001) direction. We note that, since the conventional unit cell of HfO_2 contains four Hf and eight O atoms arranged in alternating atomic planes of Hf and O, such a nonstoichiometric HfO_2 slab has a noninteger number of unit cells (5.75 in our case). We assume symmetric interface terminations, which allows us to consider two Ni/HfO_2 interfaces with polarization pointing into the Ni layer and away from the Ni layer using the same structural model with unidirectional polarization of HfO_2 (Figure 7,a). Due to the presence of polarization in HfO_2, the two interfaces have a different band alignment, and there is an associated band bending across HfO_2 due to the depolarizing field. The resulting VBO between Ni and HfO_2 is then obtained by considering the middle HfO_2 layer in the heterostructure, which corresponds to the average VBO between two structurally identical interfaces with polarizations pointing into the Ni layer and away from it.

DFT calculations are performed using the projector-augmented wave (PAW) method[71,72] implemented in the Vienna *ab initio* simulation package (VASP).[73] Generalized gradient approximation[74]

for the exchange and correlation functional and a plane-wave energy cutoff of 450 eV were used in the calculations. The in-plane lattice constant for the Ni/HfO_2 heterostructure is fixed to $a = 5.185$ Å, which is the experimental lattice constant of yttrium-stabilized zirconia.[75] Structural relaxations are performed using a $6 \times 6 \times 1$ *k*-point mesh until the forces on each atom were smaller than 0.01 eV/Å. A $10 \times 10 \times 1$ *k*-point mesh was used for self-consistent electronic structure calculations.

ASSOCIATED CONTENT

ⓈⒾ Supporting Information

The Supporting Information is available free of charge at https://pubs.acs.org/doi/10.1021/acsnano.1c05001.

    Additional information on XAS, HAXPES, MCDAD, and TEM analyses (PDF)

AUTHOR INFORMATION

Corresponding Authors

Evgeny Y. Tsymbal − *Department of Physics and Astronomy, University of Nebraska−Lincoln, Lincoln, Nebraska 68588, United States;* ⓘ orcid.org/0000-0002-6728-5480; Email: tsymbal@unl.edu

Andrei Zenkevich − *Moscow Institute of Physics and Technology, Moscow Region 141700, Russia;* ⓘ orcid.org/0000-0001-8221-1116; Email: zenkevich.av@mipt.ru

Authors

Anna Dmitriyeva − *Moscow Institute of Physics and Technology, Moscow Region 141700, Russia*

Vitalii Mikheev − *Moscow Institute of Physics and Technology, Moscow Region 141700, Russia*

Sergei Zarubin − *Moscow Institute of Physics and Technology, Moscow Region 141700, Russia*

Anastasia Chouprik − *Moscow Institute of Physics and Technology, Moscow Region 141700, Russia*

Giovanni Vinai − *Istituto Officina dei Materiali (IOM)-CNR, Laboratorio TASC, Trieste I-34149, Italy;* ⓘ orcid.org/0000-0003-4882-663X

Vincent Polewczyk − *Istituto Officina dei Materiali (IOM)-CNR, Laboratorio TASC, Trieste I-34149, Italy*

Piero Torelli − *Istituto Officina dei Materiali (IOM)-CNR, Laboratorio TASC, Trieste I-34149, Italy*

Yury Matveyev − *Deutsches Elektronen-Synchrotron, Hamburg D-22607, Germany*

Christoph Schlueter − *Deutsches Elektronen-Synchrotron, Hamburg D-22607, Germany*

Igor Karateev − *National Research Center "Kurchatov Institute", Moscow 123182, Russia*

Qiong Yang − *School of Materials Science and Engineering, Xiangtan University, Xiangtan, Hunan 411105, China;* ⓘ orcid.org/0000-0002-3235-1986

Zhaojin Chen − *School of Materials Science and Engineering, Xiangtan University, Xiangtan, Hunan 411105, China*

Lingling Tao − *Department of Physics and Astronomy, University of Nebraska−Lincoln, Lincoln, Nebraska 68588, United States*

Complete contact information is available at:
https://pubs.acs.org/10.1021/acsnano.1c05001

Notes

The authors declare no competing financial interest.

REFERENCES

(1) Eerenstein, W.; Mathur, N.; Scott, J. F. Multiferroic and Magnetoelectric Materials. *Nature* **2006**, *442*, 759.

(2) Spaldin, N. A.; Ramesh, R. Advances in Magnetoelectric Multiferroics. *Nat. Mater.* **2019**, *18*, 203.

(3) Tsymbal, E. Y. Spintronics: Electric Toggling of Magnets. *Nat. Mater.* **2012**, *11*, 12.

(4) Manipatruni, S.; Nikonov, D. E.; Young, I. A. Beyond CMOS Computing with Spin and Polarization. *Nat. Phys.* **2018**, *14*, 338.

(5) Meisenheimer, P. B.; Novakov, S.; Vu, N. M.; Heron, J. T. Perspective: Magnetoelectric Switching in Thin Film Multiferroic Heterostructures. *J. Appl. Phys.* **2018**, *123*, 240901.

(6) Scott, J. F. Data Storage. Multiferroic Memories. *Nat. Mater.* **2007**, *6*, 256.

(7) Bibes, M.; Barthélémy, A. Multiferroics: Towards a Magnetoelectric Memory. *Nat. Mater.* **2008**, *7*, 425.

(8) Martin, L. W.; Crane, S. P.; Chu, Y.-H.; Holcomb, M. B.; Gajek, M.; Huijben, M.; Yang, C.-H.; Balke, N.; Ramesh, R. Multiferroics and Magnetoelectrics: Thin Films and Nanostructures. *J. Phys.: Condens. Matter* **2008**, *20*, 434220.

(9) Velev, J. P.; Jaswal, S. S.; Tsymbal, E. Y. Multi-Ferroic and Magnetoelectric Materials and Interfaces. *Philos. Trans. R. Soc., A* **2011**, *A369*, 3069.

(10) Vaz, C. A. F. Electric Field Control of Magnetism in Multiferroic Heterostructures. *J. Phys.: Condens. Matter* **2012**, *24*, 333201.

(11) Hu, J.-M.; Duan, C.-G.; Nan, C.-W.; Chen, L.-Q. Understanding and Designing Magnetoelectric Heterostructures Guided by Computation: Progresses, Remaining Questions, and Perspectives. *npj Comp. Mater.* **2017**, *3*, 18.

(12) Nan, C.-W.; Bichurin, M. I.; Dong, S.; Viehland, D.; Srinivasan, G. Multiferroic Magnetoelectric Composites: Historical Perspective, Status, and Future Directions. *J. Appl. Phys.* **2008**, *103*, 031101.

(13) Nan, T. X.; Zhou, Z. Y.; Lou, J.; Liu, M.; Yang, X.; Gao, Y.; Rand, S.; Sun, N. X. Voltage Impulse Induced Bistable Magnetization Switching in Multiferroic Heterostructures. *Appl. Phys. Lett.* **2012**, *100*, 132409.

(14) Franke, K. J. A.; López González, D.; Hämäläinen, S. J.; van Dijken, S. Size Dependence of Domain Pattern Transfer in Multiferroic Heterostructures. *Phys. Rev. Lett.* **2014**, *112*, 017201.

(15) Wang, Q.; Li, X.; Liang, C.-Y.; Barra, A.; Domann, J.; Lynch, C.; Sepulveda, A.; Carman, G. Strain-Mediated 180° Switching in CoFeB and Terfenol-D Nanodots with Perpendicular Magnetic Anisotropy. *Appl. Phys. Lett.* **2017**, *110*, 102903.

(16) Duan, C. G.; Jaswal, S. S.; Tsymbal, E. Y. Predicted Magnetoelectric Effect in Fe/BaTiO3 Multilayers: Ferroelectric Control of Magnetism. *Phys. Rev. Lett.* **2006**, *97*, 047201.

(17) Yamauchi, K.; Sanyal, B.; Picozzi, S. Interface Effects at a Half-Metal/Ferroelectric Junction. *Appl. Phys. Lett.* **2007**, *91*, 062506.

(18) Molegraaf, H. J. A.; Hoffman, J.; Vaz, C. A. F.; Gariglio, S.; van der Marel, D.; Ahn, C. H.; Triscone, J.-M. Magnetoelectric Effects in Complex Oxides with Competing Ground States. *Adv. Mater.* **2009**, *21*, 3470.

(19) Radaelli, G.; Petti, D.; Plekhanov, E.; Fina, I.; Torelli, P.; Salles, B. R.; Cantoni, M.; Rinaldi, C.; Gutiérrez, D.; Panaccione, G.; Varela, M.; Picozzi, S.; Fontcuberta, J.; Bertacco, R. Electric Control of Magnetism at the Fe/BaTiO3 Interface. *Nat. Commun.* **2014**, *5*, 3404.

(20) Zhou, Z.; Howe, B. M.; Liu, M.; Nan, T.; Chen, X.; Mahalingam, K.; Sun, N. X.; Brown, G. J. Interfacial Charge-Mediated Non-Volatile Magnetoelectric Coupling in Co0.3Fe0.7/Ba0.6Sr0.4-TiO3/Nb: SrTiO3 Multiferroic Heterostructures. *Sci. Rep.* **2015**, *5*, 7740.

(21) Rajapitamahuni, A.; Tao, L. L.; Hao, Y.; Song, J.; Xu, X.; Tsymbal, E. Y.; Hong, X. Ferroelectric Polarization Control of Magnetic Anisotropy in PbZr0.2Ti0.8O3/La0.8Sr0.2MnO3 Heterostructures. *Phys. Rev. Mater.* **2019**, *3*, 021401.

(22) Motti, F.; Vinai, G.; Petrov, A.; Davidson, B. A.; Gobaut, B.; Filippetti, A.; Rossi, G.; Panaccione, G.; Torelli, P. Strain-Induced Magnetization Control in an Oxide Multiferroic Heterostructure. *Phys. Rev. B: Condens. Matter Mater. Phys.* **2018**, *97*, 094423.

(23) Chen, X.; Zhu, X.; Xiao, W.; Liu, G.; Feng, Y. P.; Ding, J.; Li, R.-W. Nanoscale Magnetization Reversal Caused by Electric Field-Induced Ion Migration and Redistribution in Cobalt Ferrite Thin Films. *ACS Nano* **2015**, *9*, 4210−4218.

(24) Vinai, G.; Motti, F.; Bonanni, V.; Petrov, A. Y.; Benedetti, S.; Rinaldi, C.; Stella, M.; Cassese, D.; Prato, S.; Cantoni, M.; Rossi, G.; Panaccione, G.; Torelli, P. Reversible Modification of Ferromagnetism through Electrically Controlled Morphology. *Adv. Electron. Mater.* **2019**, *5*, 1900150.

(25) Motti, F.; Vinai, G.; Bonanni, V.; Polewczyk, V.; Mantegazza, P.; Forrest, T.; Maccherozzi, F.; Benedetti, S.; Rinaldi, C.; Cantoni, M.; Cassese, D.; Prato, S.; Dhesi, S. S.; Rossi, G.; Panaccione, G.; Torelli, P. Interplay between Morphology and Magnetoelectric Coupling in Fe/PMN-PT Multiferroic Heterostructures Studied by Microscopy Techniques. *Phys. Rev. Mater.* **2020**, *4*, 114418.

(26) Manipatruni, S.; Nikonov, D. E.; Lin, C. C.; Gosavi, T. A.; Liu, H.; Prasad, B.; Huang, Y. L.; Bonturim, E.; Ramesh, R.; Young, I. A. Scalable Energy-Efficient Magnetoelectric Spin-Orbit Logic. *Nature* **2019**, *565* (7737), 35−42.

(27) Böscke, T. S.; Müller, J.; Bräuhaus, D.; Schröder, U.; Böttger, U. Ferroelectricity in Hafnium Oxide Thin Films. *Appl. Phys. Lett.* **2011**, *99*, 102903.

(28) Müller, J.; Böscke, T. S.; Schröder, U.; Mueller, S.; Bräuhaus, D.; Böttger, U.; Frey, L.; Mikolajick, T. Ferroelectricity in Simple Binary ZrO2 and HfO2. *Nano Lett.* **2012**, *12*, 4318.

(29) Zhou, D.; Müller, J.; Xu, J.; Knebel, S.; Brauhaus, D.; Schröder, U. Insights into Electrical Characteristics of Silicon Doped Hafnium Oxide Ferroelectric Thin Films. *Appl. Phys. Lett.* **2012**, *100*, 082905.

(30) Clima, S.; Wouters, D. J.; Adelmann, C.; Schenk, T.; Schröder, U.; Jurczak, M.; Pourtois, G. Identification of the Ferroelectric Switching Process and Dopant-Dependent Switching Properties in Orthorhombic HfO2: A First Principles Insight. *Appl. Phys. Lett.* **2014**, *104*, 092906.

(31) Martin, D.; Müller, J.; Schenk, T.; Arruda, T. M.; Kumar, A.; Strelcov, E.; Yurchuk, E.; Müller, S.; Pohl, D.; Schröder, U. Ferroelectricity in Si-Doped HfO2 Revealed: A Binary Lead-Free Ferroelectric. *Adv. Mater.* **2014**, *26*, 8198.

(32) Zarubin, S.; Suvorova, E.; Spiridonov, M.; Negrov, D.; Chernikova, A.; Markeev, A.; Zenkevich, A. Ultrathin Hf0.5Zr0.5O2 Ferroelectric Films on Si. *Appl. Phys. Lett.* **2016**, *109*, 192903.

(33) Tao, L. L.; Paudel, T. R.; Kovalev, A. A.; Tsymbal, E. Y. Reversible Spin Texture in Ferroelectric HfO2. *Phys. Rev. B: Condens. Matter Mater. Phys.* **2017**, *95*, 245141.

(34) Shimizu, T.; Mimura, T.; Kiguchi, T.; Shiraishi, T.; Konno, T.; Katsuya, Y.; Sakata, O.; Funakubo, H. Ferroelectricity Mediated by Ferroelastic Domain Switching in HfO2-Based Epitaxial Thin Films. *Appl. Phys. Lett.* **2018**, *113*, 212901.

(35) Wei, Y.; Nukala, P.; Salverda, M.; Matzen, S.; Zhao, H. J.; Momand, J.; Everhardt, A. S.; Agnus, G.; Blake, G. R.; Lecoeur, P.; Kooi, B. J.; Íñiguez, J.; Dkhil, B.; Noheda, B. A Rhombohedral Ferroelectric Phase in Epitaxially Strained Hf0.5Zr0.5O2 Thin Films. *Nat. Mater.* **2018**, *17*, 1095.

(36) Francois, T.; Grenouillet, L.; Coignus, J.; Blaise, P.; Carabasse, C.; Vaxelaire, N.; Magis, T.; Aussenac, F.; Loup, V.; Pellissier, C. Demonstration of BEOL-Compatible Ferroelectric Hf0.5Zr0.5O2 Scaled FeRAM Co-Integrated with 130nm CMOS for Embedded NVM Applications. *IEEE IEDM* **2019**, 362.

(37) Mueller, S.; Müller, J.; Hoffmann, R.; Yurchuk, E.; Schlösser, T.; Boschke, R.; Paul, J.; Goldbach, M.; Herrmann, T.; Zaka, A.; Schröder, U.; Mikolajick, T. From MFM Capacitors toward Ferroelectric Transistors: Endurance and Disturb Characteristics of HfO2-Based FeFET Devices. *IEEE Trans. Electron Devices* **2013**, *60*, 4199.

(38) Seo, M.; Kang, M.-H.; Jeon, S.-B.; Bae, H.; Hur, J.; Jang, B. C.; Yun, S.; Cho, S.; Kim, W.-K.; Kim, M.-S.; Hwang, K.-M.; Hong, S.; Choi, S.-Y.; Choi, Y.-K. First Demonstration of a Logic-Process Compatible Junctionless Ferroelectric FinFET Synapse for Neuromorphic Applications. *IEEE Electron Device Lett.* **2018**, *39*, 1445.

(39) Ambriz-Vargas, F.; Kolhatkar, G.; Broyer, M.; HadjYoussef, A.; Nouar, R.; Sarkissian, A.; Thomas, R.; GomezYáñez, C.; Gauthier, M. A.; Ruediger, A. A Complementary Metal Oxide Semiconductor Process-Compatible Ferroelectric Tunnel Junction. *ACS Appl. Mater. Interfaces* **2017**, *9*, 13262.

(40) Chouprik, A.; Chernikova, A.; Markeev, A.; Mikheev, V.; Negrov, D.; Spiridonov, M.; Zarubin, S.; Zenkevich, A. Electron Transport across Ultrathin Ferroelectric Hf0.5Zr0.5O2 Films on Si. *Microelectron. Eng.* **2017**, *178*, 250.

(41) Goh, Y.; Jeon, S. Enhanced Tunneling Electroresistance Effects in HfZrO-Based Ferroelectric Tunnel Junctions by High-Pressure Nitrogen Annealing. *Appl. Phys. Lett.* **2018**, *113*, 052905.

(42) Chernikova, A.; Kozodaev, M.; Markeev, A.; Negrov, D.; Spiridonov, M.; Zarubin, S.; Bak, O.; Buragohain, P.; Lu, H.; Suvorova, E.; Gruverman, A.; Zenkevich, A. Ultrathin Hf0.5Zr0.5O2 Ferroelectric Films on Si. *ACS Appl. Mater. Interfaces* **2016**, *8*, 7232.

(43) Tian, X.; Shibayama, S.; Nishimura, T.; Yajima, T.; Migita, S.; Toriumi, A. Evolution of Ferroelectric HfO2 in Ultrathin Region down to 3 nm. *Appl. Phys. Lett.* **2018**, *112*, 102902.

(44) Mikheev, V.; Chouprik, A.; Lebedinskii, Yu; Zarubin, S.; Matveyev, Yu; Kondratyuk, E.; Kozodaev, M.; Markeev, A.; Zenkevich, A.; Negrov, D. Ferroelectric Second-Order Memristor. *ACS Appl. Mater. Interfaces* **2019**, *11*, 32108.

(45) Wei, Y.; Matzen, S.; Quinteros, C. P.; Maroutian, T.; Agnus, G.; Lecoeur, P.; Noheda, B. Magneto-Ionic Control of Spin Polarization in Multiferroic Tunnel Junctions. *npj Quantum Mater.* **2019**, *4*, 62.

(46) Yang, Q.; Tao, L.; Jiang, Z.; Zhou, Y.; Tsymbal, E. Y.; Alexandrov, V. Magnetoelectric Effect at the Ni/HfO2 Interface Induced by Ferroelectric Polarization. *Phys. Rev. Appl.* **2019**, *12*, 024044.

(47) van der Laan, G.; Figueroa, A. X-Ray Magnetic Circular Dichroism A Versatile Tool to Study Magnetism. *Coord. Chem. Rev.* **2014**, *277−278*, 95−129.

(48) Ueda, S.; Tanaka, H.; Takaobushi, J.; Ikenaga, E.; Kim, J.-J.; Kobata, M.; Kawai, T.; Osawa, H.; Kawamura, N.; Suzuki, M. Hard X-Ray Photoemission Spectroscopy Combined with Magnetic Circular Dichroism: Application to Fe3-xZnxO4 Spinel Oxide Thin Films. *Appl. Phys. Express* **2008**, *1*, 077003.

(49) Matveyev, Yu; Nergov, D.; Chernikova, A.; Lebedinskii, Yu; Kirtaev, R.; Zarubin, S.; Suvorova, E.; Gloskovskii, A.; Zenkevich, A. Effect of Polarization Reversal in Ferroelectric TiN/Hf0.5Zr0.5O2/TiN Devices on Electronic Conditions at Interfaces Studied in Operando by Hard X-Ray Photoemission Spectroscopy. *ACS Appl. Mater. Interfaces* **2017**, *9* (49), 43370.

(50) Matveyev, Yu; Mikheev, V.; Negrov, D.; Zarubin, S.; Kumar, A.; Grimley, E. D.; LeBeau, J. M.; Gloskovskii, A.; Tsymbal, E. Y.; Zenkevich, A. Polarization-Dependent Electric Potential Distribution across Nanoscale Ferroelectric Hf0.5Zr0.5O2 in Functional Memory Capacitors. *Nanoscale* **2019**, *11*, 19814.

(51) Chowdhury, N.; Bedanta, S. Controlling the Anisotropy and Domain Structure with Oblique Deposition and Substrate Rotation. *AIP Adv.* **2014**, *4*, 027104.

(52) Scott, J. F.; Kammerdiner, L.; Parris, M.; Traynor, S.; Ottenbacher, V.; Shawabkeh, A.; Oliver, W. F. Switching Kinetics of Lead Zirconate Titanate Submicron Thin Film Memories. *J. Appl. Phys.* **1988**, *64*, 787−792.

(53) Chouprik, A.; Negrov, D.; Tsymbal, E. V.; Zenkevich, A. Defects in Ferroelectric HfO2. *Nanoscale* **2021**, *13*, 11635.

(54) Tuxen, A.; Carenco, S.; Chintapalli, M.; Chuang, C. H.; Escudero, C.; Pach, E.; Jiang, P.; Borondics, F.; Beberwyck, B.; Alivisatos, A. P.; Thornton, G.; Pong, W. F.; Guo, J.; Perez, R.; Besenbacher, F.; Salmeron, M. Size-Dependent Dissociation of Carbon Monoxide on Cobalt Nanoparticles. *J. Am. Chem. Soc.* **2013**, *135*, 2273.

(55) Edla, R.; Braglia, L.; Bonanni, V.; Miotello, A.; Rossi, G.; Torelli, P. Study of Gaseous Interactions on Co3O4 Thin Film Coatings by Ambient Pressure Soft X-Ray Absorption Spectroscopy. *J. Phys. Chem. C* **2019**, *123*, 24511.

(56) Montoro, L. A.; Abbate, M.; Almeida, E. C.; Rosolen, J. M. Electronic Structure of the Transition Metal Ions in LiCoO2, LiNiO2 and LiCo0.5Ni0. 5O2. *Chem. Phys. Lett.* **1999**, *309*, 14.

(57) Kuświk, P.; Gastelois, P. L.; Soares, M. M.; Tolentino, H. C. N.; De Santis, M.; Ramos, A. Y.; Lamirand, A. D.; Przybylski, M.; Kirschner, J. Effect of CoO/Ni Orthogonal Exchange Coupling on Perpendicular Anisotropy of Ni Films on Pd(001). *Phys. Rev. B: Condens. Matter Mater. Phys.* **2015**, *91*, 134413.

(58) Rode, K.; Mattana, R.; Anane, A.; Cros, V.; Jacquet, E.; Contour, J. P.; Petroff, F.; Fert, A.; Arrio, M. A.; Sainctavit, P.; Bencok, P.; Wilhelm, F.; Brookes, N. B.; Rogalev, A. Magnetism of (Zn,Co)O Thin Films Probed by X-Ray Absorption Spectroscopies. *Appl. Phys. Lett.* **2008**, *92*, 012509.

(59) Fadley, C. S. Hard X-Ray Photoemission with Angular Resolution and Standing-Wave Excitation. *J. Electron Spectrosc. Relat. Phenom.* **2013**, *190B*, 165.

(60) Schlueter, C.; Gloskovskii, A.; Ederer, K.; Schostak, I.; Piec, S.; Sarkar, I.; Matveyev, Y.; Lömker, P.; Sing, M.; Claessen, R.; Wiemann, C.; Schneider, C. M.; Medjanik, K.; Schönhense, G.; Amann, P.; Nilsson, A.; Drube, W. The New Dedicated HAXPES Beamline P22 at PETRAIII. *AIP Conf. Proc.* **2018**, *2054*, 040010.

(61) Kraut, E.; Grant, R.; Waldrop, J.; Kowalczyk, S. Semiconductor Core-Level to Valence-Band Maximum Binding-Energy Differences: Precise Determination by X-Ray Photoelectron Spectroscopy. *Phys. Rev. B: Condens. Matter Mater. Phys.* **1983**, *28*, 1965−1977.

(62) Lebedinskii, Y.; Zenkevich, A.; Gusev, E. Measurements of Metal Gate Effective Work Function by X-Ray Photoelectron Spectroscopy. *J. Appl. Phys.* **2007**, *101*, 074504.

(63) Karimzadeh, A.; Aliofkhazraei, M.; Walsh, F. C. A Review of Electrodeposited Ni-Co Alloy and Composite Coatings: Microstructure, Properties and Applications. *Surf. Coat. Technol.* **2019**, *372*, 463.

(64) Bogatyrenko, S.; Kryshtal, A.; Minenkov, A.; Kruk, A. Miscibility Gap Narrowing on the Phase Diagram of Au-Ni Nanoparticles. *Scr. Mater.* **2019**, *170*, 57−61.

(65) Vaz, C. A. F.; Staub, U. Magnetoelectronics-Electric Field Control of Magnetism in the Solid State. *J. Phys.: Condens. Matter* **2015**, *24*, 500301.

(66) Belashchenko, K. D.; Tsymbal, E. Y.; van Schilfgaarde, M.; Stewart, D.; Oleynik, I. I.; Jaswal, S. S. Effect of Interface Bonding on Spin-Dependent Tunneling from the Oxidized Co Surface. *Phys. Rev. B: Condens. Matter Mater. Phys.* **2004**, *69*, 174408.

(67) Belashchenko, K. D.; Tsymbal, E. Y.; Oleynik, I. I.; van Schilfgaarde, M. Positive Spin Polarization in Co/Al2O3/Co Tunnel Junctions Driven by Oxygen Adsorption. *Phys. Rev. B: Condens. Matter Mater. Phys.* **2005**, *71*, 224422.

(68) Vinai, G.; Ressel, B.; Torelli, P.; Loi, F.; Gobaut, B.; Ciancio, R.; Casarin, B.; Caretta, A.; Capasso, L.; Parmigiani, F.; Cugini, F.; Solzi, M.; Malvestuto, M.; Ciprian, R. Giant Magneto-Electric Coupling in 100 nm Thick Co Capped by ZnO Nanorods. *Nanoscale* **2018**, *10*, 10.

(69) Radaelli, G.; Petti, D.; Plekhanov, E.; Fina, I.; Torelli, P.; Salles, B. R.; Cantoni, M.; Rinaldi, C.; Gutiérrez, D.; Panaccione, G.; Varela, M.; Picozzi, S.; Fontcuberta, J.; Bertacco, R. Electric Control of Magnetism at the Fe/BaTiO3 Interface. *Nat. Commun.* **2014**, *5*, 3404.

(70) Panaccione, G.; Vobornik, I.; Fujii, J.; Krizmancic, D.; Annese, E.; Giovanelli, L.; Maccherozzi, F.; Salvador, F.; De Luisa, A.; Benedetti, D.; Gruden, A.; Bertoch, P.; Polack, F.; Cocco, D.; Sostero, G.; Diviacco, B.; Hochstrasser, M.; Maier, U.; Pescia, D.; Back, C. H.; et al. Advanced Photoelectric Effect Experiment Beamline at Elettra: A Surface Science Laboratory Coupled with Synchrotron Radiation. *Rev. Sci. Instrum.* **2009**, *80*, 043105.

(71) Blöchl, P. E. Projector Augmented-Wave Method. *Phys. Rev. B: Condens. Matter Mater. Phys.* **1999**, *50*, 17953.

(72) Kresse, G.; Joubert, D. From Ultrasoft Pseudopotentials to the Projector Augmented-Wave Method. *Phys. Rev. B: Condens. Matter Mater. Phys.* **1999**, *59*, 1758.

(73) Kresse, G.; Furthmüller, J. Efficient Iterative Schemes for ab Initio Total-Energy Calculations Using a Plane-Wave Basis Set. *Phys. Rev. B: Condens. Matter Mater. Phys.* **1996**, *54*, 11169.

(74) Perdew, J. P.; Burke, K.; Ernzerhof, M. Generalized Gradient Approximation Made Simple. *Phys. Rev. Lett.* **1996**, *77*, 3865.

(75) Katayama, K.; Shimizu, T.; Sakata, O.; Shiraishi, T.; Nakamura, S.; Kiguchi, T.; Akama, A.; Konno, T. J.; Uchida, H.; Funakubo, H. Orientation Control and Domain Structure Analysis of {100}-Oriented Epitaxial Ferroelectric Orthorhombic HfO2-Based Thin Films. *J. Appl. Phys.* **2016**, *119*, 134101.